THINKING BEYOND THE DATA

Turbulence-plankton interactions: a new cartoon

Peter A. Jumars[1], John H. Trowbridge[2], Emmanuel Boss[1] & Lee Karp-Boss[1]

1 School of Marine Sciences, University of Maine, Orono, ME, USA
2 Applied Ocean Physics & Engineering Department, Woods Hole Oceanographic Institution, Woods Hole, MA, USA

Abstract

Climate change redistributes turbulence in both space and time, adding urgency to understanding of turbulence effects. Many analytic and analog models used to simulate and assess effects of turbulence on plankton rely on simple Couette flow. There shear rates are constant and spatially uniform, and hence so is vorticity. Over the last decade, however, turbulence research within fluid dynamics has focused on the structure of dissipative vortices in space and time. Vorticity gradients, finite net diffusion of vorticity and small radii of curvature of streamlines are ubiquitous features of turbulent vortices at dissipation scales but are explicitly excluded from simple, steady Couette flows. All of these flow components contribute instabilities that cause rotation of particles and so are important to simulate in future laboratory devices designed to assess effects of turbulence on nutrient uptake, particle coagulation, motility and predator-prey encounter in the plankton. The Burgers vortex retains these signature features of turbulence and provides a simplified ''cartoon'' of vortex structure and dynamics that nevertheless obeys the Navier-Stokes equations. Moreover, this idealization closely resembles many dissipative vortices observed in both the laboratory and the field as well as in direct numerical simulations of turbulence. It is simple enough to allow both simulation in numerical models and fabrication of analog devices that selectively reproduce its features. Exercise of such numerical and analog models promises additional insights into mechanisms of turbulence effects on passive trajectories and local accumulations of both living and nonliving particles, into solute exchange with living and nonliving particles and into more subtle influences on sensory processes and swimming trajectories of plankton, including demersal organisms and settling larvae in turbulent bottom boundary layers. The literature on biological consequences of vortical turbulence has focused primarily on the smallest, Kolmogorov-scale vortices of length scale η. Theoretical dissipation spectra and direct numerical simulation, however, indicate that typical dissipative vortices with radii of 7η to 8η, peak azimuthal speeds of order 1 cm s^{-1} and lifetimes of order 10 s or longer (and much longer for moderate pelagic turbulence intensities) deserve new attention in studies of biological effects of turbulence.

Introduction

Marine life concentrates in two turbulent boundary layers, one just under the sea surface and one just over the sea bed. How turbulence affects marine life is a key, basic research question that also has high relevance in predicting effects of climate change. Global warming can be expected to increase mean upper-ocean stratification via temperature gradients and thereby suppress global-ocean, mean turbulence intensity. At the same time, however, it will increase turbulence intensity locally and intermittently through more energetic storm events. That

turbulence has strong effects on marine community structure has not been doubted since Margalef's seminal descriptions of its consequences for phytoplankton community structure (Margalef 1978; Margalef *et al.* 1979), but achieving a better understanding of mechanisms underlying these effects has suddenly become more urgent.

Turbulence in the upper ocean stems from shear stresses applied by wind; conversely, turbulence in the bottom boundary layer arises from friction with the sea bed. Turbulence spans broad size spectra, from the integral scale, with inertial eddies comparable in size to the 'container' (*e.g.* mixed-layer depth or bottom boundary-layer thickness), to much smaller dissipative eddies of scales on the order of millimeters, where kinetic energy is lost quickly to friction in the form of viscosity. Maximal turbulent velocities are associated with the largest eddies, and plankton by its definition moves along in them. Under high surface wind stresses, the largest and fastest of such eddies span the entire upper mixed layer and move phytoplankton cells across this layer's full spectrum of light intensities. One major consequence for phytoplankton is rapid, repeated transit through the full range of irradiances within the upper mixed layer. On this macroscopic scale that extends from the largest, most energetic eddies to scales at which dissipation begins to become important, flow and particle interact very little, and advective translation is the clear mechanism accounting for the large irradiance and pressure changes that the true plankton experiences.

We treat the opposite end of the turbulence spectrum, the dissipation scales experienced by individual phytoplankton cells, other biota and suspended particles in general, as relative motion of fluid and particle. Large, high-kinetic-energy (integral) scales and dissipation scales of turbulence are reasonably distinct (*e.g.* Gargett 1997; her Fig. 8). Concepts, models and measurements of turbulent motions at dissipative scales have evolved profoundly over the last two decades, particularly through attention to vorticity (Saffman 1992; Davidson 2004; Wu *et al.* 2006). Paradoxically, however, this substantial advance in the understanding of the physics of turbulence – despite many convincing empirical demonstrations of turbulence effects on plankton – has resulted in a substantial lag in the understanding of mechanisms, magnitudes and consequences of those effects. The reason for the lag is that on the scale of an individual phytoplankter, flow and particle interact intimately, with abundant feedbacks, and mechanisms are subtle. These mechanisms and feedbacks surely underlie some of the strong patterns on display in Margalef's mandala (Margalef 1978; Margalef *et al.* 1979).

We must make plain at the outset that we use the term 'particle' to mean a small object in the solid phase. No small mischief has been caused in the aquatic literature through ambiguity of fluid dynamicists' shorthand in referring to an infinitesimally small parcel of fluid as a 'particle.' Confusion is further amplified by referring to the trajectories of such parcels as 'particle paths' and by the fact that visualization of what are really parcel paths is often through multiple exposures or frames of small, neutrally buoyant particles seeded into the moving fluid.

The train toward increased physical understanding of turbulence has moved along on two complementary, parallel tracks, and analogous, parallel approaches have yielded greater understanding of the biological effects of turbulence. One approach includes and dissects the full complexity of turbulence through statistical analysis and summary, whereas the other deals in idealized simplifications that illuminate signature processes or mechanisms of turbulence. Each has advantages and disadvantages, and progress is most rapid when both tracks are followed, with frequent or at least occasional cross-fertilization. If both approaches are working correctly, each must be compatible with the same, accurate direct numerical simulations (DNS) of turbulence. The advantages of idealizations are succinctly encapsulated by Davidson (2004, p. 302) and underlie the title of our article: '...one might speculate that, in the decades to come, deterministic cartoons will play an increasingly important role, if only because they allow us to tap into our highly developed intuition as to the behaviour of individual vortices. We do not have the same intuitive relationship to the statistical theories, which in any event are plagued by the curse of the closure problem.' In this paper we attempt to implement this advantage while in no way questioning the value of the parallel statistical approach; we reach repeatedly onto the statistical track and especially into unifying DNS results to find realistic parameter values for our proposed cartoon.

Analog simulations aimed at testing for biological effects have also followed these two tracks. Those who seek to reproduce statistical properties of turbulence rely primarily on tanks that use flow past (static or oscillating) grids or paddles to mimic field conditions over a selected range of scales, and carry out tests for biological effects by placing organisms in tanks very much like those used to study turbulence itself. The flow history experienced by each cell in such a tank differs, but averaging over individual cells (that each integrate over both space and time) achieves empirical estimates of the magnitudes of turbulence effects at a population level. Laboratory flow tanks inevitably entail compromises in scaling of their representations of field conditions, and turbulence tanks are no exceptions (Nowell & Jumars 1987; Peters & Redondo

1997; Sanford 1997). Nevertheless, measurements in well-simulated turbulence are probably the best experimental means to test for the existence and magnitude of ecologically important turbulence effects at population levels and have achieved notable elegance in experimental implementation (*e.g.* Warnaars & Hondzo 2006).

Nagging questions in experimental design, exacerbated by the intermittency of turbulence, however, are whether cells respond cumulatively or acutely to flow effects or to durations of effects above a threshold level. Bulk assays alone cannot identify underlying mechanisms of effects on individuals. Also problematic in laboratory turbulence tanks are both strong gradients in dissipation rates with distance from the structure that sheds vortices (grid or paddle) and artifacts from direct physical contact of cells with that structure and with container walls. Nevertheless, individual particles now can be tracked long and frequently enough to generate useful statistics, *e.g.* on particle–particle encounter rates (Hill *et al.* 1992) and on net vertical velocities of slightly positively or negatively buoyant particles (Friedman & Katz 2002; Ruiz *et al.* 2004). Results have important implications, respectively, for coagulative termination of phytoplankton blooms (*e.g.* Tisalius & Kuylenstierna 1996) and for the potential of slight, physiologically controlled buoyancy changes to greatly accelerate net vertical velocities of cells in turbulence beyond values expected from Stokes settling (or rising) calculations – toward 25% of u_{rms}, the root mean square turbulent velocity (Friedman & Katz 2002). Progress is clearly being made along this statistical track in understanding effects of turbulence on plankton and will undoubtedly continue.

Here we focus on the parallel track of studies that attempt to look at simplified components or 'cartoons' of turbulence. Recent progress along this track in the physics of turbulence suggests new approaches in understanding biological effects, but we begin with a little background on development of the even more simplified models of turbulence in whose contexts biological oceanographers now study turbulence effects on plankton. This brief review allows us to develop salient differences in the new cartoon.

Background

Roles that fluid motions play in transport of solutes to and away from cells and aggregates are fundamental issues in biological and chemical oceanography. Various approaches dating back to Munk & Riley's (1952) seminal assessment have indicated that passive sinking, active swimming and ambient fluid motions each enhance fluxes of solutes to or from cells in a turbulent sea when cells

exceed a few tens of micrometers in radius. The primary mechanism is erosion or distortion of the diffusive chemical boundary layer created by the cell's uptake and release of solutes. Straining of the concentration field produces subregions of both steeper and shallower chemical gradients, but this straining typically increases net diffusive fluxes at the whole-cell scale (raises the Sherwood number; Karp-Boss *et al.* 1996). Apt analogies, because they share identical governing equations, are with electrical conduction and 'short circuits' (Murray & Jumars 2002).

Two spatial scales have figured most prominently in analyses of potential effects of small-scale motions on plankton, the Kolmogorov scale, η [L], and the Batchelor microscale, η_b [L] defined as:

$$\eta = \left(\frac{\nu^3}{\overline{\varepsilon}}\right)^{1/4} \tag{1}$$

and

$$\eta_b = \left(\frac{\nu D^2}{\overline{\varepsilon}}\right)^{1/4} \tag{2}$$

Here $\overline{\varepsilon}$ [L$^2\cdot$T^{-3}] represents the spatially and temporally averaged rate of turbulent dissipation of kinetic energy, ν [L$^2\cdot$T^{-1}] is the kinematic viscosity and D [L$^2\cdot$T^{-1}] is the molecular diffusion coefficient of the solute molecule in question. We employ the unusual notation (overbar) for mean dissipation rate because we will later argue that phytoplankton and other suspended and swimming organisms are most affected by larger, local dissipation rates (ε_{loc}), which we will attempt to quantify. Because we rely in part on scaling arguments, upon first introduction of each parameter we use the physics convention of indicating its primary dimensions in square brackets. The first parameter, η, estimates the diameter of the smallest vortices that turbulence can support in the face of viscosity, whereas η_b estimates the scale of the smallest solute concentration gradient that fluid motion will support in the face of molecular diffusion. Both are scaling arguments, so the right side of each carries an implicit constant that has to be estimated from data (Gargett 1997), but the leading coefficients are often omitted (as above) for simplicity.

Mixed-layer turbulent dissipation rates typically range between approximately 10^{-5} and 10^{-9} m$^2\cdot$s^{-3}, kinematic viscosity is within a factor of two of 10^{-6} m$^2\cdot$s^{-1}, and D is generally one or two times 10^{-9} m$^2\cdot$s^{-1} for small solute molecules such as nitrate, giving ranges of 0.6–6 mm for η and 18–180 μm for η_b. We extend the 'typical' upper mixed layer range for dissipation rates an order of magnitude upward from our prior review (Karp-Boss *et al.* 1996) based on recent measurements that succeeded in

dissecting wave from turbulent motions (Gerbi *et al.* 2008, 2009). Diatoms are roughly 5–1000 μm long as individual cells and chains, and in still water at steady state have chemical boundary layers (concentration deviation of >10% from background) extending (for a spherical cell), 10 cell radii from the cell's center (Karp-Boss *et al.* 1996). Thus, from equations (1) and (2), large, individual cells and even longer chains and larger colonies clearly can experience consequences of shear- and vorticity-generated gradients in both relative velocity (cell *versus* surrounding fluid) and dissolved nutrient concentration. Large, motile dinoflagellates themselves can produce sufficient flow past their surfaces to enhance solute fluxes over magnitudes that would hold in the absence of their swimming, but shear impedes this process (Karp-Boss *et al.* 1996, 2000; Durham *et al.* 2009). Colonial flagellates also can enhance net supply of nutrients by producing relative fluid motion when ambient flows are weak (Solari *et al.* 2006), but again turbulence may interfere, in this case by rapidly altering pressure distributions around the colony.

We focus on phytoplankton because of its central role in biological oceanography, but turbulent dissipation is also of interest in many other contexts. Those other contexts greatly expand the dissipation rates of potential interest (*cf.* Thorpe 2007), from the lowest values in mid waters of deep oceans (10^{-10} m$^2 \cdot$s^{-3}) to maxima in surf zones and tidal channels (10^{-1} m$^2 \cdot$s^{-3}). We do not extend our analysis to these ranges, but the methods we present can be used to do so. We do briefly touch upon bottom boundary layers because of their relative simplicity and rich history of study. In shallow waters the upper mixed layer and bottom boundary layer can be one and the same, with surface or bottom effects dominating in inverse proportion to distance from those respective boundaries.

Many experimental tests of flow effects on phytoplankton have been based on the seminal review and analysis by Lazier & Mann (1989), who noted that phytoplankton cells are generally smaller than the diameters of the smallest coherent vortices of dissipating turbulence, η. They argued from a characteristic profile of velocity *in one dimension* that viscosity will rapidly produce a roughly linear velocity gradient (thus constant shear and vorticity) over the scale of ∼1 mm, so that phytoplankton (and much smaller bacteria) spend most of their time in simple shear flows. The basis of this argument is well founded for laminar flows whose velocities vary in a single dimension; just as concentration profiles in one dimension approach linearity in steady state through diffusion of mass (governed in rate by the diffusion coefficient, D), velocity profiles in one dimension approach linearity in steady state through diffusion of momentum

(governed in rate by the diffusion coefficient for momentum, or kinematic viscosity, ν). This assessment or 'cartoon' has formed the basis for numerous experimental studies of 'turbulence' effects on plankton in simple Couette flows (*e.g.* Thomas & Gibson 1990; Latz *et al.* 1994; Shimeta *et al.* 1995; Karp-Boss & Jumars 1998). This linear gradient in velocity was coupled by Lazier & Mann (1989) with their more subtle assessments that the level of shear (steepness of the velocity gradient) varies randomly in time within a range specified by a universally observed spectrum of shear energy density and that the direction of the shear in homogeneous turbulence varies randomly over all three spatial dimensions.

Perhaps the most useful measure of scientific understanding is the capacity to make and verify interesting alternative predictions (*i.e.* predictions not already generally accepted to be true or false). Prediction has come through engineering models for simple, engineered flows, primarily steady, laminar shears that fit Lazier & Mann's (1989) summary of the phytoplankter's environment very well. Predictions have used analytic models of trajectories and rotation rates (Jeffery 1922) and semi-empirical estimates of flux enhancements of nutrients, based on empirical relationships between Sherwood and Péclet numbers (reviewed by Karp-Boss *et al.* 1996) and, sometimes, numerical models (Pahlow *et al.* 1997). That important insights have been gained is undeniable, yet some key aspects of turbulence have gone missing in the linear-shear cartoon. It is time for the next step in complexity toward greater realism.

Vortical motion

Textbook-level understanding of millimeter to centimeter scales of turbulent flows has diverged rapidly from the suggestion that typical flow at the scale of a phytoplankter comprises steady shear and constant vorticity. Instead, the idea that a turbulent flow is a writhing tangle of vortex 'worms' better describes results of observations and DNS (Fig. 1). Fluid dynamicists now dare to define turbulence rather than continue to diagnose it from a syndrome of characteristics: irregularity, diffusivity, large Reynolds numbers, three-dimensional vorticity fluctuations, dissipation, and adherence to continuum mechanics (*cf.* Tennekes & Lumley 1972). Davidson (2004, p. 53) has defined hydrodynamic turbulence in an incompressible fluid as 'a spatially complex distribution of vorticity which advects itself in a chaotic manner in accordance with (2.31) [reproduced below as equation (3)]. The vorticity field is random in both space and time, and exhibits a wide and continuous distribution of length and time scales.' Wu *et al.* (2006, p. 106) attribute an even simpler definition of turbulence to Bradshaw: 'randomly stretched vortices.'
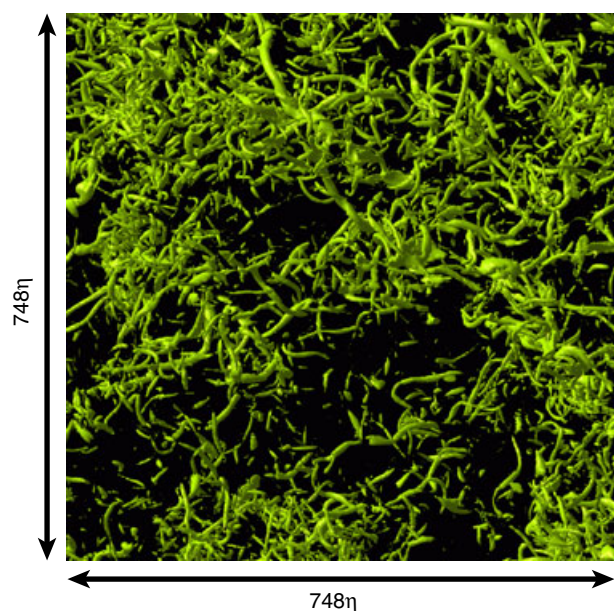
Fig. 1. A writhing tangle of 'vortex worms': Isosurfaces of intense vorticity, showing regions where the absolute value of vorticity exceeds by over four standard deviations its mean value. The symbol η is the Kolmogorov length scale [equation (1)] and the visualized depth (third Cartesian dimension) of the simulation is 1496 η. The Taylor Reynolds number, Re_λ for this direct numerical simulation (DNS) is 732 [*cf.* equation (18)]. Reproduced by permission of the authors and IEEE [© IEEE (2002) from p. 17 of Yokokawa *et al.* (2002), their Fig. 7].

Vorticity, vortices and stretching (straining) are essential components of the new fluid dynamics 'cartoon.'

Reynolds numbers are dimensionless and have the general form of a speed (u) times a length scale (l) times a fluid density (ρ), all divided by a dynamic viscosity (μ). The two fluid properties are often combined into a kinematic viscosity, $\nu = \mu/\rho$, reducing the number of terms to three: ul/ν. Variety in Reynolds numbers (Re) is limitless and depends on choice of length and speed scales. A generally useful body Re for particle motion chooses particle radius as the length scale and relative speed of the particle to that of the far-field surrounding fluid as the speed scale. We later will also introduce two more Reynolds numbers specific to vortices. Re can be interpreted generally as the ratio between inertial and viscous forces within a specific flow. Higher Re implies greater turbulence intensity.

Before we introduce additional equations, we should comment on notation. Vorticity, ω, is a vector quantity, but only magnitude and not direction of rotation in isotropic turbulence is important to our arguments, and at dissipation scales in intense, isotropic turbulence there is no bias of one direction of rotation over the other. Therefore, we largely avoid the added distraction of vector notation, with the single exception of Fig. 2, where direction determines sign. There and elsewhere, we completely arbitrarily show velocity profiles for counterclockwise-rotating vortices (looking at them from the top), which by the right-hand convention makes vorticity positive. Half the vortices in isotropic turbulence will oppose that direction of rotation; we work far below the scale where Coriolis effects become significant.

Evaluation of turbulence effects on organisms clearly has not reached the new, vorticity-focused, textbook-level understanding of turbulence. Steady, Couette flow by design is one dimensional, with constant shear orthogonal to the driving surface(s). Toward the goal of simplicity in representation and analysis, vorticity is constrained to be parallel to the driving surface(s). The vorticity equation (where both ω and u are vectors) can be written as

$$\frac{D\omega}{Dt} = (\omega \cdot \nabla)u + \nu\nabla^2\omega. \qquad (3)$$

It is sound practice to start with a simplified mathematical basis, make sure that everything works, and interpret those results and their limitations before moving toward the realism and added complexity of fully 3D solutions and time variation. For turbulence, however, the path *must* be followed into 3D because in 2D the first term on the right of equation (3) equals zero, so only viscous forces (through diffusion of vorticity via the second term on the right) can alter vorticity in a 2D flow. In 2D, signature features of turbulence at dissipation scales thus are missing: Vortex stretching cannot occur, and any vorticity is confined to the axis orthogonal to the two dimensions of the system that are explicitly modeled. In steady Couette flow, vorticity shows no net diffusion because it is constant throughout; both terms on the right are exactly zero. In and near real vortices, however, vorticity diffuses down gradients. Couette flow can produce realistic views neither of the deformations that vortical flows produce in both chemical boundary layers and plumes nor of translation, rotation and deformation of cells and chains caused by fluid motion in and near vortices.

By definition, vortices are coherent fluid motions in the two dimensions perpendicular to their axes rather than random or chaotic fluctuations in all three spatial dimensions. Vortical stirring can bring reactants together in ways that random fluctuations cannot (Crimaldi *et al.* 2006), with abundant ecological consequences (*e.g.* Crimaldi & Browning 2004). The high shear and diffusing vorticity between a dissipative eddy and its surrounding medium are likely to have profound effects on small organisms. The question that we pursue here is how to select and utilize a physical cartoon of dissipative-scale vortices to improve understanding of turbulence effects on those organisms.
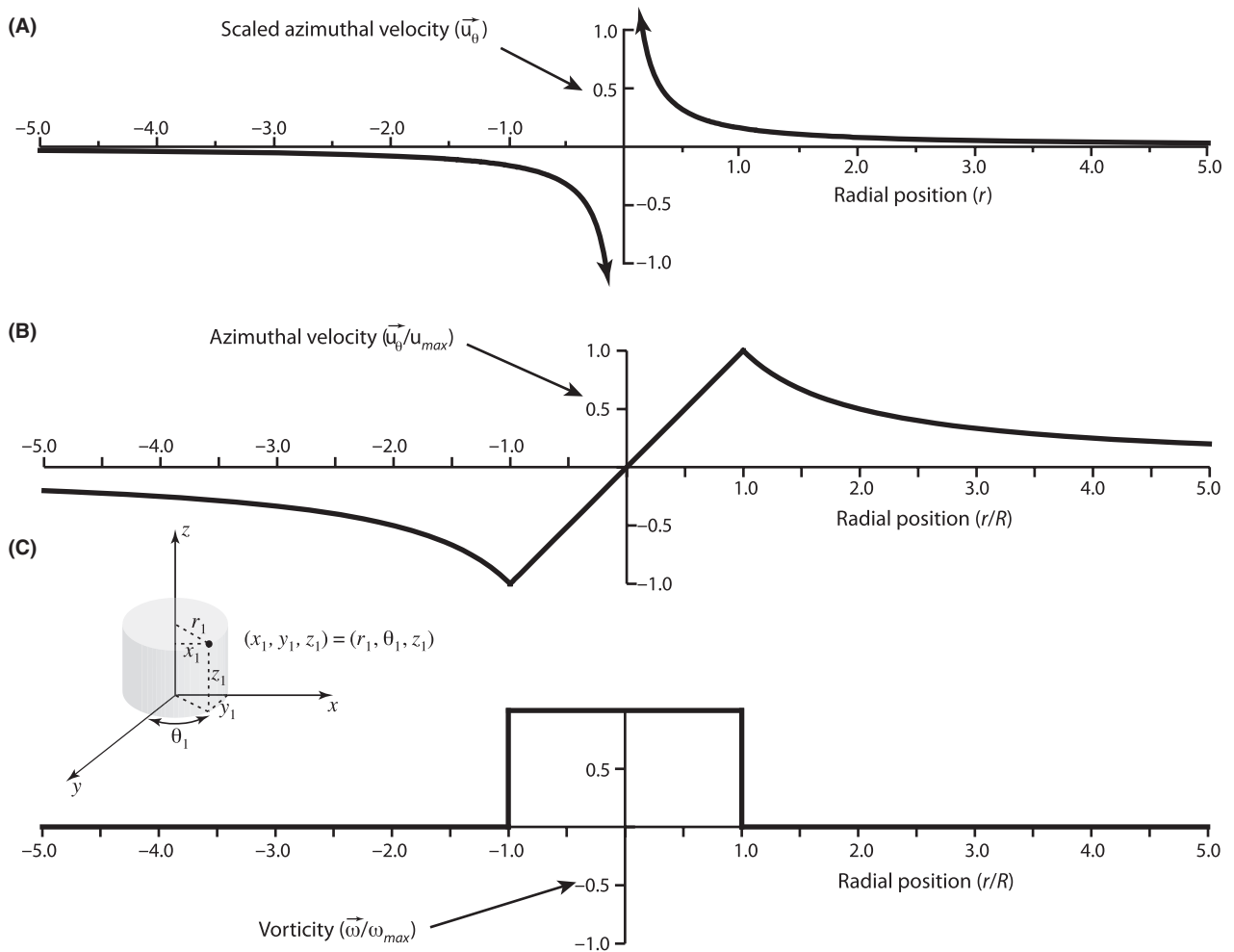
Fig. 2. (A) Scaled azimuthal velocity, u_θ, *versus* distance, r, from the vortex center in a line vortex. To get azimuthal velocity from the graph, one would need to multiply values on the ordinate by the circulation, Γ. That velocity approaches $-\infty$ and $+\infty$, respectively from the left and the right of the origin as the vortex center is approached. All of the line vortex's vorticity exists at $r = 0$. (B) Azimuthal velocity *versus* distance, r, from the vortex center in a Rankine combined vortex. The core of radius R rotates as a solid body, $u_\theta = ru_{\theta max}/R$, for $|r| \leq R$, whereas azimuthal velocity decreases beyond the core as $u_\theta = Ru_{\theta max}/r$ for $|r| > R$. (C) Vorticity in a Rankine combined vortex *versus* distance, r, from the vortex center is constant for the core, $|r| \leq R$, and zero elsewhere. The abscissa in (B) and (C) is non-dimensionalized by dividing by the vortex radius, R. Ordinates in (B) and (C) were non-dimensionalized by dividing by their respective maximal magnitudes. Idealized vortices of these sorts are inviscid, and all initial vorticity is conserved. There are no velocity components in the radial or axial (z) directions. The inset (between B and C) illustrates the cylindrical coordinates that we use (r, θ, z) and the representation of an arbitrary point in both cylindrical and Cartesian coordinates. Some authors use ϕ in place of θ and ρ in place of r. We follow the usual convention that counterclockwise rotation is associated with positive vorticity (right-hand rule) but arbitrarily show velocity and vorticity for counterclockwise vortices (panels A and B having the perspective of looking at the vortex from above, *i.e.* from the positive z direction). Analogous panels (A–C) for clockwise vortices can be generated by reflection of each illustrated curve about its abscissa. In isotropic turbulence, there is no bias toward vortices of positive or negative vorticity.

Axial symmetry is appropriate for the simplest vortex cartoon. The natural coordinate system is z for distance along axis, r for distance perpendicular to that axis and θ for angular (azimuthal) position about the axis. Before we consider realistic vortex structures at dissipation scales, we work through a succession of vortex cartoons of increasing complexity, a line vortex, a Rankine combined vortex, the intuitive but complex 'bathtub vortex' and one simplified viscous vortex. The simplest vortices are

inviscid. In the absence of viscosity, the second term on the right of equation (3) equals zero, so only vortex stretching (or its opposite) can alter vorticity. Inviscid vortices provide useful contrasts with vortices that are substantially affected by viscosity.

Our first vortex cartoon is the idealized line vortex (*e.g.* Batchelor 1967), in which both axial and radial velocity components are zero, axial vorticity is concentrated in a singularity at the origin ($r = 0$), and azi-

muthal velocity, u_θ (Fig. 2A), is given by $\Gamma/(2\pi r)$, where Γ [$L^2 \cdot T^{-1}$] is vortex strength or circulation, defined formally as the line integral around a closed path surrounding the origin in the r–θ plane. [Acheson (1990) provides a highly accessible introduction to the concept of circulation and its application.] Viscous terms in the equation of motion are identically zero for $r > 0$ in the idealized line vortex.

Our second vortex cartoon is the Rankine combined vortex, so named because the central core behaves very differently from the outer flow field (Fig. 2B, C). Flow again is exclusively azimuthal. Velocity increases linearly from the center of the vortex to a maximum, $u_{\theta max}$, at the outer edge of the core (defined as $r = R$). The region $r < R$ lacks shear. In this core, all motion is as though in solid-body rotation, i.e. as if the water and everything suspended in it were frozen and spinning literally like a top. Vorticity in the core therefore is constant and falls abruptly to zero beyond R, where azimuthal velocity falls off as $u_{\theta max}/r$. Tornadoes and dust devils often approximate this structure. As they left Kansas, Dorothy and Toto remained at a constant distance from and in fixed orientation to each other, while each was spun around to face each compass point exactly once in each complete rotation of the tornado. This kind of vortex also has relevance to plankton and the larger scales of turbulence, whose statistics generated by DNS can be surprisingly well simulated by invoking a spectrum of inertial-scale, randomly oriented, Rankine vortices (He *et al.* 1999). The combined Rankine vortex requires that the fluid be inviscid, so that the second term on the right of equation (3) equals zero. Inviscid vortices are useful as simpler end members to contrast with flows that are substantially affected by viscosity.

Our third vortex cartoon, perhaps the most familiar but also the most complex in this series of three, forms when a large tub of water drains through a relatively small opening in its bottom in the presence of system rotation at angular velocity Ω [T^{-1}]. (If the tub is fixed to the rotating earth, then Ω is the local vertical component of the angular velocity of the earth; if the tub is fixed to a rotating laboratory table, then Ω is the angular velocity of the table). At large scale ($\sqrt{\nu/\Omega}$ small compared with the water depth and tub radius), inward radial velocity toward the drain is confined primarily to a relatively thin 'Ekman' layer of thickness $\sqrt{\nu/\Omega}$ over the tub bottom, and vertical velocity is confined primarily to the narrow core of the vortex (Andersen *et al.* 2003). Outside of the vortex core and away from the tub boundaries, viscosity is again unimportant, and azimuthal velocity u_θ is given approximately by $\Omega\, r + \Gamma/r$, where the vortex strength Γ is given in this case by $F\sqrt{\Omega/\nu}/\pi$, with F [$L^3 \cdot T^{-1}$] being the volume flow rate exiting the tub

(Andersen *et al.* 2003). Vertical flow produced by gravity is providing the vortex stretching. Where Ωr is small, as in a common bathtub, u_θ is approximately Γ/r, so its profile with r resembles that of a line vortex (Fig. 2A). In a bathtub vortex, the radial pressure gradient is apparent as a depression of steeply increasing depth toward the vortex center.

We introduce this relatively complex vortex because it connects a commonly experienced flow with the otherwise abstract idea of vortex stretching as a means to accelerate azimuthal flow. It also dramatically visualizes the otherwise nearly invisible role of pressure in vortical flow at small scale. Lower-than-ambient pressure along the axis is common to all small vortices but is blatantly obvious only in the bathtub vortex. Whether its vorticity is positive or negative – even for a weakly spinning, viscous vortex – careful examination of the water surface will reveal a dimple where a vortex axis intersects the water surface. Low pressure provides the centripetal forces that keep the fluid from following a straight path. The spinning liquid itself exerts the centrifugal forces that dynamically maintain this same negative pressure, and the overall dynamic stability of net forces in the spinning fluid underlies the clear prevalence of vortices in turbulence (Fig. 1).

The presence of viscosity

Viscosity destroys singularities and local steepness in one-dimensional velocity gradients. The simplest viscous vortex can be described as a desingularization of a line vortex (Lamb 1932; Batchelor 1967), and is termed the Lamb–Oseen vortex by Saffman (1992), who gives analytic solutions for the resultant, circular velocity and vorticity fields. These solutions are consistent with the Navier–Stokes equations. Viscous diffusion acts quickly on small scales to move u_θ as a function of r toward Gaussian shape. For an initial circulation, Γ_0, concentrated at the origin (Saffman 1992, p. 253):

$$u_\theta = \frac{\Gamma}{2\pi r} = \frac{\Gamma_0}{2\pi r}\left(1 - e^{-r^2/4\nu t}\right); \qquad (4)$$

$$\omega_z = \frac{\Gamma_0}{4\pi r \nu t} e^{-r^2/4\nu t}; \qquad (5)$$

$$\Gamma = \Gamma_0\left(1 - e^{-r^2/4\nu t}\right). \qquad (6)$$

Here t is time. To be perfectly clear, Lamb–Oseen and line vortices are identical and *do* have a singularity at $r = 0$, $t = 0$, before viscosity has had time to act, but vis-

cosity will erase the singularity in less than a millisecond. Small, axisymmetric vortices that lack any driving forces to keep them spinning differently will spin down toward this shape under the influence of viscosity no matter whether they begin as line vortices, Rankine vortices or something more complex. Their characteristic Gaussian shape in radial velocity and vorticity profiles results from the way that momentum and vorticity diffuse away from axial regions of high values in a cylindrical geometry.

Two vortical structures have emerged repeatedly from both very accurate DNS of turbulence and model simplifications. Both are consistent with the Navier–Stokes equations. The first is the Burgers (1948) vortex (Fig. 3) that accommodates extensional straining along its axis of vorticity and for realistic conditions satisfies the Navier–Stokes equations. The opposite pattern of straining (one compressional strain rate and orthogonal extensional straining along the other two axes) appears to be even more common (Davidson 2004) and produces vortex sheets. They are unstable, however (as evidenced by the dominance of vortices over sheets in Fig. 1), and tend to roll up and evolve into something approximating the second kind of vortex, the Lundgren (1982) stretched-spiral vortex, for which asymptotic solutions are available (Pullin & Saffman 1998). For diagrams of the bursting and folding steps, see Davidson (2004, p. 207). Furthermore, the Lundgren stretched-spiral vortex decays asymptotically toward the structure of the Burgers vortex (Pullin & Saffman 1998), justifying our focus here on the latter as a simplifying cartoon. Prevailing structures in turbulence clearly are elongate vortices (axial length >> radius, Fig. 1).
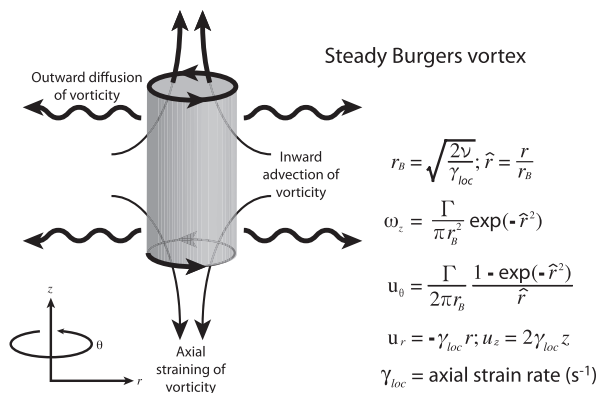

Fig. 3. Cartoon of a steady Burgers (1948) vortex. Constant tensile straining at rate γ_{loc} would accelerate the rotation (conserving vorticity) by thinning the vortex (reducing its radius) if outward diffusion of vorticity did not counterbalance this effect. Vorticity remains steady because its constant diffusion outward is counterbalanced exactly by the combination of inward advection and vortex stretching. Modified from Acheson (1990, p. 188) and Davidson (2004, p. 249).

Views regarding the applicability of the Burgers (1948) vortex have changed remarkably through DNS. Not long ago (*e.g.* Acheson 1990) this Navier–Stokes solution was considered a curiosity because no obvious spatial and velocity scales emerged with it. Hatakeyama & Kambe (1997), however, found that an ensemble of Burgers vortices with random orientations and strengths provides an accurate description of longitudinal structure functions observed in laboratory measurements and DNS of homogeneous, isotropic turbulence at dissipative scales, provided that a realistic probability density function for vortex strengths is incorporated in the calculation. In spite of limitations pointed out by He *et al.* (1999), the random Burgers vortex model thus is a potentially useful idealization for studying interactions between turbulence and plankton at dissipative scales.

In a steady Burgers vortex, viscous dissipation continuously removes kinetic energy from the flow, but velocities remain constant because a constant, local, axial strain at rate, γ_{loc} [T^{-1}], continuously accelerates the fluid azimuthally. [Note that Davidson (2004]) and some other authors use $\alpha/2$ in place of γ_{loc}; we reserve α for the dimensionless Kolmogorov constant.] Through continuity, inward radial flow supports this axial straining. Inward advection of vorticity and of azimuthal momentum by this flow balances their outward diffusion. In a steady Burgers vortex,

$$r_B = \sqrt{\frac{2\nu}{\gamma_{loc}}}; \qquad (7)$$

$$\gamma_{loc} = \frac{2\nu}{r_B^2} \qquad (8)$$

(Davidson 2004). Axial vorticity, tangential velocity and local dissipation rates show characteristic shapes as functions of non-dimensional radius, $\hat{r} = r/r_B$ (He *et al.* 1999; Fig. 4 herein):

$$u_\theta = \frac{\Gamma}{2\pi r_B}\left(\frac{1 - e^{-\hat{r}^2}}{\hat{r}}\right); \qquad (9)$$

$$\omega_z = \frac{\Gamma}{\pi r_B^2} e^{-\hat{r}^2}; \qquad (10)$$

$$u_r = -\gamma_{loc} r; \qquad (11)$$

$$u_z = \gamma_{loc} z. \qquad (12)$$

Local dissipation rate, ε_{loc}, was calculated following Hatakeyama & Kambe (1997) as:

$$\varepsilon_{loc} = \nu \left\{ 12\gamma_{loc}^2 + \left(\frac{\Gamma}{\pi r_B^2}\right)^2 \left[e^{-\widehat{r}^2} - \frac{1}{\widehat{r}^2}\left(1 - e^{-\widehat{r}^2}\right)\right]^2 \right\}. \quad (13)$$

Both vorticity and azimuthal velocity as functions of radial distance in a Burgers vortex resemble smoothed versions of those in a Rankine combined vortex (Fig 4). Local dissipation rate (zero for the Rankine), on the other hand, is large where the velocity difference between the combined Rankine and the Burgers is large, roughly in the region between r_B and $2r_B$ (Fig 4). Thus the regions in which dissipation is substantial surround and are three or more times the volume of the high-vorticity core regions visualized in the DNS of Fig. 1. Note that the central core of high vorticity has low shear and approximates solid-body rotation. A Burgers vortex may leave steady state through various mechanisms, including changes in γ_{loc}. If γ_{loc} increases, the vortex radius will shrink, and tangential velocities will accelerate, with time scale γ_{loc}^{-1} (Davidson 2004, p. 250). If γ_{loc} drops to zero, then the vortex decays, following the equations for the Lamb–Oseen vortex. If γ_{loc} shifts from positive to negative, azimuthal velocities are decelerated, potentially generating vortex sheets along an extensional plane orthogonal to the compressive straining.

Characteristic scaling of a Burgers vortex

To make the Burgers vortex cartoon useful, its parameters, r_B, γ_{loc} and Γ, must be estimated. To estimate r_B, following Gargett's (1997) lead, we first ask the size of the vortices that account for the most dissipation, *i.e.* those at the peak of the dissipation spectrum. Tennekes & Lumley (1972), their Eq. 8.4.7) give the viscous dissipation rate of kinetic energy, ε_ν, based on the Pao model as a function of wavenumber, k:

$$\varepsilon_\nu(k) = 2\alpha\nu\overline{\varepsilon}^{2/3}k^{1/3}\exp\left[-\frac{3}{2}\alpha(k\eta)^{4/3}\right]. \quad (14)$$

Note that this equation uses mean dissipation rate, $\overline{\varepsilon}$, to estimate scale-specific dissipation rates. Based on extensive DNS (Gotoh *et al.* 2002), we set α, known as the Kolmogorov constant, at 1.64. Taking the derivative of equation (14) with respect to k and finding where it is zero, locates the wavenumber at which dissipation is maximal, *i.e.* $k_d = 0.18/\eta$. A wavenumber, k, is defined as $2\pi/$diameter, consistent with both circular geometry and Fourier transformation (*cf.* Tennekes & Lumley, p. 259). The diameter at the peak in the dissipation spectrum becomes
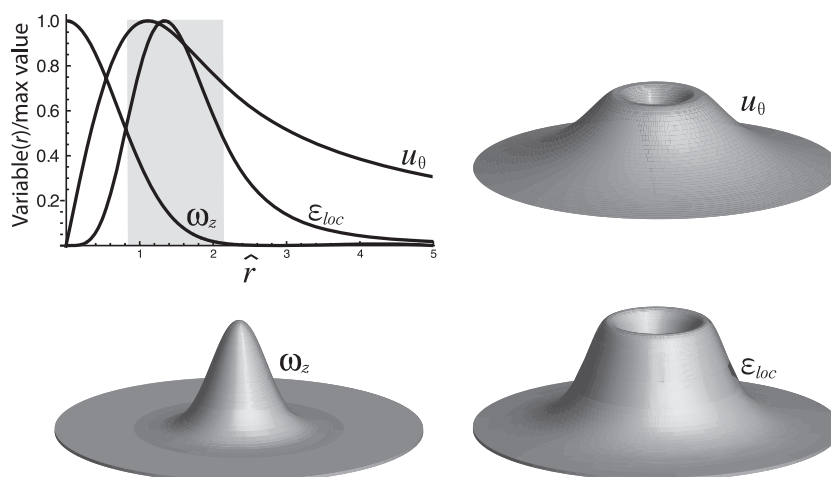

Fig. 4. Characteristic profiles of azimuthal velocity (u_θ), vorticity (ω_z), and local dissipation rate (ω_{loc}) as functions of non-dimensional radial distance, $\widehat{r}$, from the center of a steady Burgers vortex. Each curve is non-dimensionalized by dividing by its maximum value. Note that azimuthal velocity of a Burgers vortex peaks at $1.12\widehat{r}$. The gray region on the graph marks the radial distance interval in which local dissipation rate is $\geq$ 50% of its maximal value. For simplicity we have omitted values in the other half of the vortex (for negative values of $\widehat{r}$) in this and subsequent figures, but here we also show 3D visualizations of each variable (magnitude only, not direction) to emphasize the vortical structure. Azimuthal velocity in this domain can be obtained by reflecting the graph shown here about both axes, whereas vorticity and local dissipation rate can be obtained by reflection about the ordinate alone.

$$d = 11\pi\eta. \tag{15}$$

The corresponding radius, a more useful measure of distance for our subsequent purposes, is 17.5η. By integrating equation (14) with respect to k, we also calculate that 90% of dissipation occurs in the eddy radius range of 2.7η to 58η. One-half of the dissipation is associated with vortices >8.1η in radius. Because equation (14) and most other distributions that we will treat are asymmetric, we choose to use median rather than mean values as being 'typical'; although 8.1η is not a median radius, it applies a similarly tail-insensitive method to deal with the asymmetry of equation (14). Once r_B is determined ($d/2$), equation (8) reveals the local strain rate, γ_{loc}, required to maintain a Burgers vortex of that radius in steady state. The path to Γ estimates is a bit more circuitous.

Taylor (1921) introduced λ, later named the Taylor microscale, as an intermediate spatial scale at which dissipation rate, kinetic energy of the flow, and viscosity all interact:

$$\bar{\varepsilon} = 15\nu\frac{u_{rms}^2}{\lambda^2}; \tag{16}$$

$$\lambda = \sqrt{\frac{15\nu}{\bar{\varepsilon}}}\, u_{rms} \tag{17}$$

(*e.g.* Frisch 1995; Eq. 2.28 and 5.10). It falls between dissipation and integral length scales. To connect Taylor's derivation with equations (16) and (17), we make use of the equality of $\bar{\varepsilon}$ and $\nu\overline{\omega_i\omega_i}$, where ω_i is the ith component of vorticity (*e.g.* Frisch 1995, p. 21), in Frisch's expression for λ. The length and velocity scales, in turn, can be used to form a Taylor Reynolds number,

$$Re_\lambda = \frac{u_{rms}\lambda}{\nu}, \tag{18}$$

that further characterizes flow at this intermediate scale where inertial energy is spilling into the dissipation spectrum. Kolmogorov (1941) hypothesized that small-scale turbulence statistics depend on $\bar{\varepsilon}$ and ν alone, but – because of intermittency – these two parameters have proven insufficient to determine u_{rms} (Frisch 1995). That is, the same $\bar{\varepsilon}$ can result from flows that vary in intermittency and hence in u_{rms}. We therefore need a way to choose an appropriate u_{rms}.

Direct numerical simulations have revealed statistical regularities that aid in estimating the remaining Burgers vortex parameter and use the quantities in equations (16)–(18). Hatakeyama & Kambe (1997) sought to analyze the distribution of vortex Reynolds numbers, Re_Γ, defined as

$$Re_\Gamma = \frac{\Gamma}{\nu}. \tag{19}$$

They assumed for isotropic turbulence that mean strain rate

$$\bar{\gamma} = \frac{u_{rms}}{2\lambda}, \text{and} \tag{20}$$

$$\Gamma = 2\pi r_B u_{rms} \tag{21}$$

Consequently, the mean value for the fraction is

$$\frac{Re_\Gamma}{\sqrt{Re_\lambda}} = 4\pi. \tag{22}$$

Hatakeyama & Kambe (1997) found that equation (22) fits the central tendency for previously published DNS very well, supporting our use of equation (21) to estimate Γ. They used DNS results further to characterize the distribution of Re_Γ about this mean tendency and proposed that the Re_Γ has a probability density function, $P_{Re_\Gamma}(Re_\Gamma)$, given by

$$P_{Re_\Gamma}(Re_\Gamma) = \frac{C^3}{2}Re_\Gamma^2 \exp(-CRe_\Gamma), \tag{23}$$

where, in order to conform to equation (22),

$$C = \frac{3}{4\pi\sqrt{Re_\lambda}}. \tag{24}$$

The expression for C in note [21] of Hatakeyama & Kambe (1997) contains a typographical error that has been corrected here. The expected or mean value of Re_Γ based on the model distribution is $4\pi Re_\lambda^{1/2}$, as per equation (22). Ninety percent of Re_Γ values would fall between 0.27 and 2.1 times that mean value, however, and the same proportional range from its mean would be expected for Γ [equation (19)]. The most frequent (modal) Re_Γ and Γ are two-thirds of their respective mean values, whereas the medians are 0.89 times the means.

He *et al.* (1999) adopted the Hatakeyama & Kambe (1997) distribution of Re_Γ and further proposed, based on previously published DNS, that the dimensionless Burgers radius, $\tilde{r} = r_B/\eta$, has a probability density, P_{Γ_B}, given by

$$P_{\Gamma_B}(\tilde{r}_B) = E\tilde{r}_B^2 \exp(-\tilde{r}_B^{0.7}). \tag{25}$$

E in turn is a normalization constant given by

$$E^{-1} = \int_0^{+\infty} \tilde{r}_B^2 \exp(-\tilde{r}_B^{0.7}) d\tilde{r}_B. \qquad (26)$$

The expected value (mean) of r_B based on this approach is approximately, 8.5η and the median is 7.1η, both remarkably close to the median-like value of 8.1η obtained from the dissipation spectrum. Good correspondence of these two approaches in identifying a 'typical' Burgers vortex radius gives some confidence that the choice is a good one, and each approach also permits examination of the broader spectrum of dissipation-scale vortices. Ninety percent of Burgers vortex radii under equation (25) fall between 1.8η and 20η.

We first estimate the parameters of the Burgers vortex in the simplest and longest-studied kind of boundary layer, *i.e.* the boundary layer produced by steady, horizontally uniform, unidirectional (in the mean) flow over wall or sea floor of uniform roughness, a so-called 'wall layer.' In a crude way, a bottom boundary layer is kinematically similar to an upside-down upper mixed layer. It is simpler in some ways because the geometry of the sediment-water interface evolves more slowly than the air–sea interface. The presence of the more-or-less rigid wall, however, creates some important differences. Following the normal convention, we use positive x for the downstream direction, y for the cross-stream dimension and z for the vertical dimension, and u, v and w for the respective velocity components. Here we will use u, v and w explicitly to refer to the fluctuating components of velocity (elsewhere often denoted with an apostrophe). We follow the usual convention of z being positive upward from the sea bed. Vorticity is generated at the sea bed in the y direction and has the same direction of rotation as would a bicycle tire rolling downstream over the sea bed. In proximity to the wall, turbulent vortices retain some of this bias toward rotating about a cross-stream axis, and vertical velocities are suppressed by the low-permeability wall.

As a specific example, we consider the wall layer of an unstratified bottom boundary layer. The ensemble-averaged dissipation is approximately (*e.g.* Thorpe 2007, p. 86)

$$\bar{\varepsilon} = \frac{u_*^3}{\kappa z}, \qquad (27)$$

where u_* is the shear velocity and $\kappa \simeq 0.41$ is von Kármán's constant. Shear velocity is estimated from vertical profiles of horizontal velocity (*e.g.* Gross & Nowell 1983). Following Monin & Yaglom (1971, p. 280), standard deviations of the velocity components are

$$\left[\left(\overline{u^2} \right)^{1/2}, \left(\overline{v^2} \right)^{1/2}, \left(\overline{w^2} \right)^{1/2} \right] \simeq [2.3, 1.7, 0.9] u_*, \qquad (28)$$

so that

$$u_{rms} \simeq \left[\frac{1}{3} \left(2.3^2 + 1.7^2 + 0.9^2 \right) \right]^{1/2} u_* \simeq 1.7 u_*. \qquad (29)$$

For $\nu = 10^{-6}$ m$^2\cdot$s^{-1}, $u_* = 10^{-2}$ m$\cdot$s^{-1} (a value near the critical erosion threshold for many unconsolidated sediments) and $z = 2.5$ m, equation (27) yields $\bar{\varepsilon} = 9.8 \times 10^{-7}$ m$^2\cdot$s^{-3}. Further, $\eta = 1.0 \times 10^{-3}$ m [equation (1)], $r_B \simeq 7.1$ mm [7.1η, median of equation (25)], $u_{rms} \simeq 1.7 \times 10^{-2}$ m$\cdot$s^{-1} [equation (29)], $\lambda \simeq 6.7 \times 10^{-2}$ m [equation (17)] and $Re_\lambda \simeq 1.1 \times 10^3$ [equation (18)]. The remaining Burgers parameters become $\gamma_{loc} = 3.9 \times 10^{-2}$ s^{-1} [equation (8)] and $\Gamma = 7.6 \times 10^{-4}$ m$^2\cdot$s^{-1} [equation (21)]. Using median values of the proposed distribution [equation (23)], one finds $Re_\Gamma \simeq 3.8 \times 10^2$. With these values, the Burgers vortex solution [equation (9)–(13)] gives max $(u_\theta) \simeq 1.1$ cm$\cdot$s^{-1}, max $(\varepsilon_{loc}) \simeq 2.1\bar{\varepsilon}$ and max $(\omega_z) \simeq 4.8$ s^{-1}.

Estimation of the Burgers vortex parameters in an upper mixed layer can be complicated by the interaction of gravity waves with turbulent motions. Such interactions have been the subject of extensive research. Here we use simplified results based on recent field measurements and scaling arguments to provide quantitative estimates of the relevant scales; the results do not account explicitly for quasi-coherent processes such as Langmuir circulations (*e.g.* Thorpe 2007), although these processes are likely incorporated in the empirical results.

Significant wave height, H_s [m] is the vertical peak-to-trough distance. When waves break, motions within this region (with the interface $z = 0$ defined as the midpoint between peak and trough and increasing depth being considered positive z) are very time- and location-dependent. The region from the wave trough to a depth of order $10H_s$ is called the wave-affected surface layer. Unlike the classic wall model, where turbulent kinetic energy comes entirely from vertical shear, in this region turbulent kinetic energy derives primarily from downward transport of kinetic energy injected by waves breaking above (Gerbi *et al.* 2009, their Fig. 1). In the wave-affected surface layer, mean dissipation rate can be written

$$\bar{\varepsilon} = 0.3 \frac{G_t u_*^3 H_s}{z^2}, \qquad (30)$$

where H_s is the significant wave height and G_t is a dimensionless parameter that expresses the ratio between u_*^3 and the energy flux from the wind to the waves, which ranges between approximately 90 and 250 for all but extremely young seas (Terray *et al.* 1996). Gerbi *et al.* (2009) found that a value of 168 provided the best fit of their observations to the scaling of Terray *et al.* (1996). Terray *et al.* (1996), Drennan *et al.* (1996), Feddersen *et al.* (2007), Jones & Monismith (2008), and Gerbi *et al.* (2009)

showed that equation (30) describes near-surface dissipation in a variety of field measurements. Burchard (2001) showed that an appropriately modified, two-equation turbulence model [equation (30) for the wave-affected layer and equation (27) for the layer below it] reproduces the observed dissipation structure. Gerbi *et al.* (2009) found field measurements of velocity variance in the wave-affected surface layer to be consistent with

$$q^3 = \Lambda \bar{\varepsilon} z, \tag{31}$$

where $q^2 = (1/2)\left(\overline{u^2} + \overline{v^2} + \overline{w^2}\right)$ is the turbulent kinetic energy per unit of mass and Λ is an empirical constant with a median value of approximately 1.34. Measurements of $\overline{w^2}$ reported by Gerbi *et al.* (2009) are consistent with those of D'Asaro (2001) and Tseng & D'Asaro (2004). It follows from the above expression and the definitions of q^2 and u_{rms} that in the wave-affected surface layer

$$u_{rms} = \left(\frac{2}{3}\right)^{1/2} (\Lambda \bar{\varepsilon} z)^{1/3}. \tag{32}$$

Terray *et al.* (1996) estimated that the wave-affected surface layer is bounded by

$$0.6 \leq \frac{z}{H_s} \leq 0.3 \kappa G_t. \tag{33}$$

The upper bound is obtained by equating the expressions for dissipation in the wave-affected surface layer and wall layer. Depth of the transition varies with time since onset of wind and peaks at intermediate wave age, when it can be as large as $25H_s$ (Terray *et al.* 1996, their Fig. 8).

We use the Gerbi *et al.* (2009) results to produce a sample calculation. We emphasize that these results are by no means extreme and are limited to significant wave heights of about 1 m or less at the Martha's Vineyard Cabled Observatory (MVCO) off the coast of Massachusetts, USA, during October 2003, in waters about 15 m deep. Data are available online at http://www.whoi.edu/mvco/data/oceandata.html. From the temperature and salinity, we estimate a kinematic viscosity of about 1.14×10^{-6} m²·s⁻¹. Gerbi *et al.* (2009, their Fig. 6) observed several episodes when $\bar{\varepsilon}$ in the wave-affected layer reached 10^{-5} m²·s⁻³. From equation (32), we obtain an estimate of $u_{rms} = 2.6$ cm·s⁻¹. Values of u_{rms} this large are supported by both the measurements of Gerbi *et al.* (2009) and estimates from float data by Tseng & D'Asaro (2004) for the open-ocean North Pacific in the same season (October–November, when kinematic viscosities, dominated by temperature, were also similar). During this season, mixed-layer depth is gradually increasing, and

stratification plays no large role in dynamics near the air–water interface. We estimate median r_B [7.1η from equation (1)] to be 4.4 mm and λ [equation (17)] to be 3.4 cm. Strain rate [equation (8)] for a steady Burgers vortex of this radius is 0.12 s⁻¹ and circulation, $\Gamma = 7.2 \times 10^{-4}$ m²·s⁻¹ [equation (21)]. With these values, the Burgers vortex solution [equation (9)–(13)] gives max $(u_\theta) \simeq 1.7$ cm·s⁻¹, max $(\varepsilon_{loc}) \simeq 1.4$ $\bar{\varepsilon}$ and max $(\omega_z) \simeq 12$ s⁻¹.

How long does this typical Burgers vortex last? To gain some idea, we calculate its decay by noting that a vortex with identical azimuthal velocity and axial vorticity can be produced by viscous decay from a line vortex that has initial circulation, Γ_0, equal to the steady value of Γ for the Burgers vortex in question (Davidson 2004, Problem 5.3, p. 291). This equivalence is most easily demonstrated by noting that the Burgers equations for azimuthal velocity and axial vorticity can be recovered by substituting the quantity $r_B^2/4\nu = \gamma_{loc}^{-1}/2$ for t in equations (4) and (5) (representing an e-folding time, *i.e.* the time to decay to $1/e$ or about 0.37 times the initial value). This necessary correspondence allows calculation of decay dynamics under the scenario of a steady Burgers vortex for which strain rate, γ_{loc}, goes instantaneously to zero (Fig. 5A–C). We set initial (time-zero) circulation at $\Gamma_0 = 7.6 \times 10^{-4}$ m²·s⁻¹ and find [equation (4)] that it takes 4.3 s to decay to the azimuthal velocity profile of our typical Burgers vortex. We observe that a natural time scale for decay of a Burgers vortex, τ_d, once straining has stopped is the inverse of the strain rate that is needed to keep it in steady state, *i.e.* $\tau_d = 1/\gamma_{loc} = 8.5$ s for the upper mixed-layer example. Because we have deliberately chosen very energetic upper mixed-layer turbulence, this time is unusually short. For the bottom boundary-layer example τ_d is substantially longer (26 s) because median r_B is somewhat larger.

All these values are remarkably larger than intuition might suggest from working at the Kolmogorov scale [equation (1)]. For explicit comparison, the Kolmogorov time scale, τ_η, and velocity scale, u_η, for this upper mixed-layer example are:

$$\tau_\eta = \left(\frac{\nu}{\varepsilon}\right)^{1/2} = 0.34 \text{ s}; \tag{34}$$

$$u_\eta = (\nu \varepsilon)^{1/4} = 1.8 \text{ mm} \cdot \text{s}^{-1}. \tag{35}$$

Better intuition comes from inspection of equation (8). The time scale for decay is proportional to the square of the vortex radius and inversely proportional to twice the kinematic viscosity. This observation helps to explain why eddies of the size at the mode of equation (14) are sub-
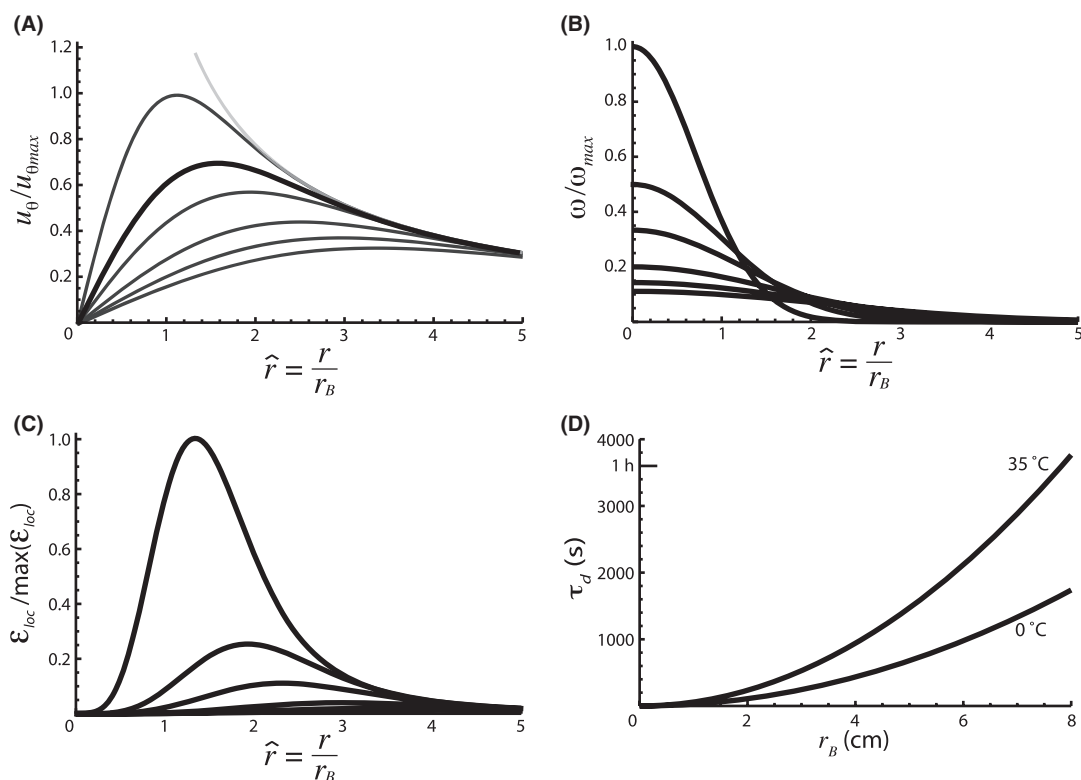
(A)

(B)

(C)

(D)

Fig. 5. Decay of a Burgers vortex when axial straining stops abruptly. For panels (A–C), top black curves show the steady value and subsequent falloff after $\tau_d/2$, τ_d, $2\tau_d$, $3\tau_d$ and $4\tau_d$, where decay time, τ_d, is defined as $1/\gamma_{loc}$, and all curves are scaled to their maximum value for the steady Burgers vortex and plotted against non-dimensionalized radial distance. (A) Azimuthal velocity. The gray line shows velocity for the corresponding Lamb–Oseen vortex at time zero. (B) Vorticity. (C) Local dissipation rate. (D) Decay time, τ_d, *versus* initial Burger's radius, r_B. The top curve is for a kinematic viscosity, ν, of 0.85×10^{-6} $m^2 \cdot s^{-1}$, whereas the bottom curve is for $\nu = 1.84 \times 10^{-6}$ $m^2 \cdot s^{-1}$. Most sea water kinematic viscosities fall between them.

stantially larger than the median or mean eddy size. Larger dissipative eddies last *much* longer (Fig. 5D). Differences produced by kinematic viscosity in these time scales also increase with vortex radius (Fig. 5D). Kinematic viscosities of sea water depend primarily on temperature and vary a little more than twofold from 0.85×10^{-6} to 1.84×10^{-6} $m^2 \cdot s^{-1}$ as temperature changes from 35 °C to 0 °C. The vortex radius at the mode of the dissipation spectrum for the upper mixed-layer conditions above is $17.5\eta = 1.1$ cm, and its time scale for decay is 55 s. Moreover, we have chosen a case of quite energetic turbulence, and typical eddy size would be larger under less energetic conditions. At low mixed-layer turbulence intensities of 10^{-9} $m^2 \cdot s^{-3}$, for example, typical and modal eddy sizes would be 10 times larger [equation (1)], and decay times consequently 100 times longer, than our upper mixed-layer example.

For our calculations of dissipation rate in the decaying vortex we go backward a step in Hatakeyama & Kambe (1997) derivation of equation (13). First we note that contributions to dissipation from straining have fallen to

zero, so the first term inside parentheses in equation (13) also is zero. All shear is radial when the axial straining stops. We calculate ε_{loc} from u_θ as

$$\varepsilon_{loc} = \nu \left(\frac{du_\theta}{dr} - \frac{u_\theta}{r} \right)^2. \qquad (36)$$

For the Burgers cases we consider, strain directly [via the first term inside parentheses of equation (13)] contributes an inconsequential fraction of the total dissipation.

Similarly, Burgers velocities are dominated by their azimuthal components (Fig. 6). The small, inward radial flow of a steady Burgers vortex, however, combines with the larger azimuthal velocity to produce a tight, inward spiraling, with many rotations before the axis is reached. The spiral becomes even tighter closer to the vortex axis (Fig. 6). The smaller the vortex and the larger the axial strain, the larger becomes the inward component relative to the azimuthal.
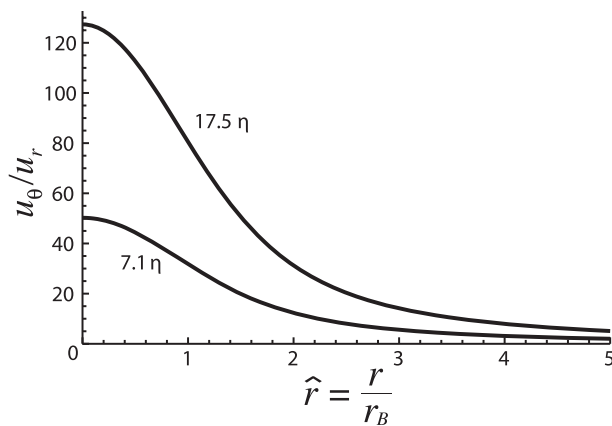
Fig. 6. Ratio of azimuthal to inward radial flow speeds *versus* scaled (non-dimensional) radial distance. Both are for vortices under the upper mixed-layer conditions discussed in the text, but one is for a Burgers radius of median size (7.1η), whereas the other is chosen to match the vortex size scale of the mode in the dissipation spectrum [17.5η, equation (14)]. Net 2D motion forms a tight inward spiral.

Some caveats are in order. Myopic focus on a single eddy diameter and velocity scale is unwise, which is why we present the spectral formula for dissipation and probability density functions for vortex radius and circulation. Vortices also clearly interact with each other in important ways, as even casual examination of Fig. 1 attests. Adjacent, counter-rotating vortices will translate together, and may join to form a single, toroidal vortex, analogous to a smoke ring in air (*e.g.* Thorpe 2007; his Fig. 1.9). The pair will have lower shear between them than would exist at the same radius from a single vortex of comparable size and velocity, and they will pull water between them as they migrate. Co-rotating vortices move in orbits around each other and may coalesce to form a larger vortex, but – until they do – they will have greater shear between them than would exist at comparable radial distance from a single vortex of similar size and rotation rate. Deformations of groups of smaller vortices by larger ones that entwine them are evident in Fig. 1; multiple-vortex interactions are present in much variety and will cause local and ephemeral extremes in strain rates, shear and dissipation. Somewhat paradoxically, these complications remove some of the early objections to Burgers vortices as representations of realistic physical entities. In the context of DNS, continued growth of velocity in the radial and axial directions implied by equations (11) and (12) is cut off by the action of instabilities in the form of higher velocities imposed by neighboring vortices (Fig. 1).

All of these interactions will affect vortex lifetimes and create extensive variation in local vorticities and dissipation rates. The cartoon of a single vortex of a given size and velocity is simply a logical place to start to examine vortex interactions with plankton. It should continue to

be complemented by studies of building complexity and by studies along the statistical track.

Planktonic interactions with the cartoon vortex

Because we began with the simpler structure of a bottom boundary layer, we also begin with a brief interpretation of turbulence effects there. Settling larvae of limited swimming capabilities are known to exploit suppressed vertical velocities by swimming downward upon detection of settling cues (*e.g.* Hadfield & Koehl 2004). Here we suggest that they also exploit near-sea bed vortices of characteristic scale and orientation. Grünbaum & Strathmann (2003) have shown that changing offsets of centers of buoyancy and centers of gravity during development can bias larvae into either updrafts (favorable for dispersal in early larval states) or downdrafts (favorable for settlement). Regions of vortices in particular orientations both in the pelagic realm and near the bottom are those updrafts and downdrafts, respectively. Another possibility in interpreting benthic organism form and function is that scales of benthic suspension feeders or their feeding appendages may be matched to characteristic vortex radii and tuned to vortex velocities.

In terms of phytoplankton in steady, uniaxial shear, elongate and discoidal cells spend most of their time aligned parallel to the velocity vectors. They tumble with predictable frequency (Jeffery 1922), and these tumbles are key in shedding diffusive boundary layers and contributing to nutrient uptake (Pahlow *et al.* 1997). Based on our prior experience with Jeffery orbits in Couette flow and in particular with our experience in unsteady Couette flows where there are diffusion gradients of shear and vorticity (Fig. 7), and thus where both velocity and vorticity change with time at any particular location, we predict that non-spherical particles in the region between one and two Burgers radii from the axis will tumble much more often than in a steady, linear shear. Inward radial flow into steady Burgers vortices and into Burgers vortices whose axial strain rates are accelerating is also of relevance in moving the cells themselves into different portions of the vortex. Clearly the Burgers vortex is a more accurate cartoon of natural turbulence than is Couette flow.

In atmospheric sciences, it is generally accepted that isotropic turbulence can act size selectively to increase droplet–droplet collision rates, to increase droplet fall velocities and to produce particle distributions that are nonrandom in space (*e.g.* Ghosh *et al.* 2005). A relevant criterion is the Stokes number, *Stk,* the non-dimensional ratio of the time that it takes a particle to respond to a change in fluid flow velocity relative to the time scale over which fluid velocity itself changes, so *Stk* << 1 indicates that particles will follow streamlines closely; at small
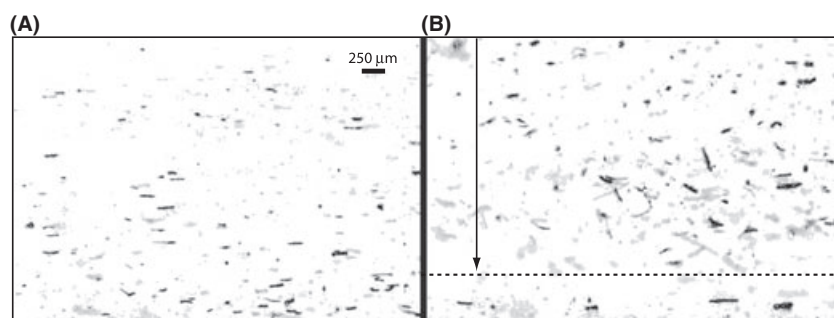
Fig. 7. (A) Alignment of diatom chains (*Stephanopyxis turris,* with chains approximately 250 μm long) perpendicular to shear in steady Couette flow. In a laminar shear orthogonal to both rotating surfaces, elongate objects spend most of their time aligned with the velocity vectors but undergo periodic Jeffery (1922) orbits (*e.g.* Pahlow *et al.* 1997; Karp-Boss & Jumars 1998). (B) The upper moving boundary recently has been accelerated, and unsteady diffusion of momentum and vorticity in the direction of the arrow has reached approximately to the dashed line. Note the dramatic effect on trajectories of chains, with known effects on surrounding nutrient boundary layers and nutrient fluxes (Pahlow *et al.* 1997). Similar tumbling can be expected in the near vicinity of dissipation-scale vortices. The chains were illuminated with white light and visualized through a red filter *via* their autofluorescence. The photographs were opened in Adobe Photoshop CS4 in RGB mode. They were converted to grayscale through the Image > Adjustments > Black&White panel by setting reds to 100% and all other colors to zero. The image was then inverted to make the brightest red autofluorescence the darkest black. All pixels with detectable red autofluorescence are shown; darker pixels had higher fluorescence intensity, and only the longer objects are phytoplankton chains. Long, dark-black objects are chains that are in focus. Long, gray objects are chains that are somewhat out of focus. Globular material comprises coagulated debris and chains. Greater coagulation evident in (B) is partly a function of time (B being later than A) but also a function of greater coagulation with greater tumbling, elongate particles each sweeping out a larger volume as they tumble.

Stk, fluid motion controls particle motion. Particle–flow interaction will be strongest for *Stk* near unity. $Stk \gg 1$, on the other hand, indicates that the particle will move through a vortex before it can respond to the local fluid motion; at large *Stk,* particle motion dominates over fluid motion. Centrifuging of negatively buoyant water droplets for *Stk* near unity increases their fall velocities and contributes to droplet growth (collision of smaller droplets) through two mechanisms. It lowers particle abundance in vortices and raises particle concentrations outside them. Because collision rates go up non-linearly with droplet concentration (*i.e.* with concentration squared), locally increased concentrations raise encounter and coagulation rates. Response of particles to turbulent fluctuations also generally increases particle relative velocities and thus encounter rates over those that would occur in still air from differential deposition alone (Vaillancourt & Yau 2000; Bosse *et al.* 2006; Ghosh *et al.* 2005).

In aquatic particle dynamics, where the ratio of particle to fluid densities is generally smaller, the contribution of isotropic turbulence to non-random particle redistribution has been more controversial since the spotlight put on this issue by Squires & Yamazaki (1995). In a steady Burgers vortex, azimuthal velocity is so much larger than the inward radial flow (Fig. 6) that particles with *Stk* above a critical value will tend to find a stable radius at which to orbit the axis, although vortex orientation with respect to the gravitational vector matters when the particles are not neutrally buoyant (Marcu *et al.* 1995). At even higher *Stk,* particles have sufficient inertia to be expelled from the vortex (Ijzermans & Hagmeijer 2006). Particles with small Stokes numbers, on the other hand, are concentrated in the strain-dominated regions of the flow (Bec *et al.* 2006;. Even neutrally buoyant spheres of non-zero Stokes number apparently can move differentially from the surrounding flow (Tallapragada & Ross 2008), although this topic remains controversial.

Much of the controversy stems from the oversimplification of particles in the modeling done for some of these studies that makes them 'point particles' that have finite mass but infinitesimal size and no explicit shape. This simplification cannot capture interactions of particle with ambient flow accurately, particularly when particle sizes approach or even exceed η (*cf.* Hill *et al.* 1992). Rarely are all the unsteady terms, especially the wake history terms, included in calculating particle trajectories. For large phytoplankton cells and chains, wake history terms can be particularly important, and their inclusion would increase *Stk* for the cells (Koehl *et al.* 2003). The ultimate reason for these simplifications is computational; DNS is difficult, and realistic incorporation of particle material properties and geometries and interactions with the flow in DNS is still forbidding in terms of the numbers of computations needed for realistic simulation.

Gopalan *et al.* (2008) put phytoplankton into isotropic turbulence. They presented a video during the 2008 Ocean Sciences Meeting in Orlando, FL, USA, of a vortex being stretched (−γ increasing in absolute value), with phytoplankton being concentrated along its axis in the process. The underlying mechanism has not been clearly

identified. For positively buoyant cells, centripetal acceleration might account for this concentration, or it might be due to the strain mechanism identified by Bec *et al.* (2006), or both. Shape effects also undoubtedly affect phytoplankton trajectories in and near vortices.

Velocities of a centimeter per second and dimensions of one to a few centimeters are also relevant to the swimming and settling dynamics of small plankton, at least up to the scales of fishes preying on copepods. That is, the vortex radii we calculate are comparable to detection distances of copepods by fishes (*e.g.* Viitasalo *et al.* 1998), and azimuthal velocities are comparable to or larger than copepod cruising and sinking speeds but not as large as copepod escape velocities (Buskey *et al.* 2002; Kiørboe 2008). Interaction with vortices is sure to affect the transition from ballistic to diffusive trajectories of plankton (Kiørboe & Visser 2005); swimming tracks cannot be independent of streamlines. Vortices quite obviously prevent organisms from swimming straight through their diameters or other secants unless swimming speeds greatly exceed flow speeds encountered in the vortex. Turbulence affects encounter of both inanimate particles and organisms (*e.g.* Hill *et al.* 1992; Visser & MacKenzie 1998), so it should not be surprising that dissipative vortices also have an effect.

Feasibility of numerical and analog testing

Although more complex than simple, linear shear, a Burgers vortex is well within current numerical modeling capabilities, so a logical way to proceed in testing effects on passive particles such as diatoms is to embed realistically shaped and mechanically behaved model diatoms and diatom chains in numerical models of a Burgers vortex. Specifically, such objects can be embedded through immersed boundary methods (Peskin 2002) and seeded in various positions and orientations in and near the vortex. Such numerical experiments can be used to isolate particular regions of the vortex and parameter combinations that lead to interesting tumbling behaviors, for example, or to local concentrations of phytoplankton.

With numerical predictions in hand, it becomes much more feasible to conduct experiments in analog devices. Small devices already have been built to allow production of a vortex between two parallel and synchronously rotating, circular plates. By drawing fluid through holes in the two respective centers of those plates, vortex stretching can be achieved (Petitjeans 2003). With commercially available software (*e.g.* COMSOL, Burlington, MA, USA), it is also now feasible to design small chambers a few centimeters long in which particular combinations of shear, vorticity and streamline curvature duplicate selected components of vortical flow. Indeed, such experiments have

already been done at slightly smaller scale and lower *Re* (Marcos & Stocker 2006).

Conclusions

Our simple calculations in the context of the new cartoon have changed the way that we think about turbulence by expanding possibilities for what we conceive as mechanistic turbulence effects over what we could imagine with the Lazier & Mann (1989) simplification. In a bottom boundary-layer setting, fish that exceed vortex diameters in length can exploit vortices that they do not themselves generate to gain energetic advantage in swimming (Liao *et al.* 2003). Detecting a vortex, its axial orientation and its direction of rotation are more difficult tasks for organisms smaller than the vortex, but if resources, predators and prey are nonrandomly distributed with respect to vortex coordinates, selection is likely to have found cues that lead individuals toward enhanced resources and away from enhanced risks. It would indeed be surprising if a copepod did not know its way around the ubiquitous features that are dissipative vortices (Fig. 1 herein; Fig. 4 of Yamazaki 1993).

Acknowledgements

References

Acheson D.J. (1990) *Elementary Fluid Mechanics*. Oxford University Press, Oxford.

Andersen A., Bohr T., Stenum B., Rasmussen J.J., Lautrup B. (2003) Anatomy of a bathtub vortex. *Physical Review Letters* **91**, 104502-1–104502-4. doi: 10.1103/PhysRevLett.91.104502

Batchelor G.K. (1967) *An Introduction to Fluid Dynamics*. Cambridge University Press, Cambridge.

Bec J., Biferale L., Boffetta G., Celani A., Cencini M., Lanotte A., Musacchio S., Toschi F. (2006) Acceleration statistics of heavy particles in turbulence. *Journal of Fluid Mechanics*, **550**, 349–358.

Bosse T., Kleiser L, Meiburg E. (2006) Small particles in homogeneous turbulence: settling velocity enhancement by two-way coupling. *Physics of Fluids*, **18**, 02712.

Burchard H. (2001) Simulating the wave-enhanced layer under breaking surface waves with two-equation turbulence models. *Journal of Physical Oceanography*, **31**, 3133–3145.

Burgers J.M. (1948) A mathematical model illustrating the theory of turbulence. *Advances in Applied Mechanics*, **1**, 171–199.

Buskey E.J., Lenz P.H., Hartline D.K. (2002) Escape behavior of planktonic copepods in response to hydrodynamic disturbances: high speed video analysis. *Marine Ecology Progress Series*, **235**, 135–146.

Crimaldi J.P., Browning H.S. (2004) A proposed mechanism for turbulent enhancement of broadcast spawning efficiency. *Journal of Marine Systems*, **49**, 3–18.

Crimaldi J.P., Hartford J.R., Weiss J.B. (2006) Reaction enhancement of point sources due to vortex stirring. *Physical Review E,* **74**, 016307.

D'Asaro E. (2001) Turbulent vertical kinetic energy in the ocean mixed layer. *Journal of Physical Oceanography*, **31**, 3530–3537.

Davidson P.A. (2004) *Turbulence: An Introduction for Scientists and Engineers*. Oxford University Press, Oxford.

Drennan W.M., Donelan M.A., Terray E.A., Katsaros K.B. (1996) Ocean turbulence dissipation measurements in SWADE. *Journal of Physical Oceanography*, **26**, 808–815.

Durham W.M., Kessler J.O., Stocker R. (2009) Disruption of vertical motility by shear triggers formation of thin phytoplankton layers. *Science*, **323**, 1067–1070.

Feddersen F., Trowbridge J.H., Williams A.J. III (2007) Vertical structure of dissipation in the nearshore. *Journal of Physical Oceanography*, **37**, 1764–1777.

Friedman P.D., Katz J. (2002) Mean rise rate of droplets in isotropic turbulence. *Physics of Fluids*, **14**, 3059–3073.

Frisch U. (1995) *Turbulence*. Cambridge University Press, Cambridge.

Gargett A.E. (1997) 'Theories' and techniques for observing turbulence in the ocean euphotic zone. *Scientia Marina*, **61** (Suppl. 1), 25–45.

Gerbi G.P., Trowbridge J.H., Edson J.B., Plueddemann A.J., Terray E.A., Fredericks J.J. (2008) Measurements of momentum and heat transfer across the air-sea interface. *Journal of Physical Oceanography*, **38**, 1054–1072.

Gerbi G.P., Trowbridge J.H., Terray E.A., Plueddemann A.J., Kukulka T. (2009) Observations of turbulence in the ocean surface boundary layer: energetics and transport. *Journal of Physical Oceanography*, doi: 10.1175/2008Jp04044.1, in press.

Ghosh S., Dávilla J., Hunt J.C.R., Srdic A., Fernando H.J.S., Jonas P.R. (2005) How turbulence enhances coalescence of settling particles with applications to rain in clouds. *Proceedings of the Royal Society of London. Series A: Mathematical and Physical Sciences*, **461**, 3059–3088.

Gopalan B., Malkiel E., Karp-Boss L., Sheng J., Katz J. (2008) Diffusion of particles in isotropic turbulence using high speed digital holographic cinematography. *Ocean Sciences Meeting abstract http://www.sgmeet.com/aslo/orlando2008/viewabstract2.asp?AbstractID=3210*.

Gotoh T., Fukayama D., Nakano T. (2002) Velocity field statistics in homogeneous steady turbulence obtained using a high-resolution direct numerical simulation. *Physics of Fluids*, **14**, 1065–1081.

Gross T.F., Nowell A.R.M. (1983) Mean flow and turbulence scaling in a tidal boundary layer. *Continental Shelf Research*, **2**, 109–126.

Grünbaum D., Strathmann R.R. (2003) Form, performance and trade-offs in swimming and stability of armed larvae. *Journal of Marine Research*, **61**, 659–691.

Hadfield M.G., Koehl M.A.R. (2004) Rapid behavioral responses of an invertebrate larva to dissolved settlement cue. *Biological Bulletin*, **207**, 28–43.

Hatakeyama N., Kambe T. (1997) Statistical laws of random strained vortices in turbulence. *Physical Review Letters*, **79**, 1257–1260.

He G., Doolen G.D., Chen S. (1999) Calculation of longitudinal and transverse velocity structure functions using a vortex model of isotropic turbulence. *Physics of Fluids*, **11**, 3743–3748.

Hill P.S., Nowell A.R.M., Jumars P.A. (1992) Encounter rate by turbulent shear of particles similar in diameter to the Kolmogorov scale. *Journal of Marine Research*, **50**, 643–668.

Ijzermans R.H.A., Hagmeijer R. (2006) Accumulation of heavy particles in a bounded vortex flow. In: Balachandar S., Prosperetti A. (Eds), *IUTAM Symposium on Computational Approaches to Multiphase Flow*. Springer, Netherlands: 75–85.

Jeffery G. B. (1922) The motion of ellipsoidal particles immersed in a viscous fluid. *Proceedings of the Royal Society of London. Series A: Mathematical and Physical Sciences*, **102**, 161–179.

Jones N. L., Monismith S.G. (2008) The influence of whitecapping waves on the vertical structure of turbulence in a shallow estuarine environment. *Journal of Physical Oceanography*, **38**, 1563–1580.

Karp-Boss L., Jumars P.A. (1998) Motion of diatom chains in steady shear. *Limnology and Oceanography*, **43**, 1767–1773.

Karp-Boss L., Boss E., Jumars P.A. (1996) Nutrient fluxes to planktonic osmotrophs in the presence of fluid motion. *Oceanography and Marine Biology, An Annual Review*, **34**, 71–107.

Karp-Boss L., Boss E., Jumars P.A. (2000) Effects of shear on swimming by dinoflagellate individuals and chains. *Limnology and Oceanography*, **45**, 1594–1602.

Kiørboe T. (2008) *A Mechanistic Approach to Zooplankton Ecology*. Princeton University Press, Princeton.

Kiørboe T., Visser A.W. (2005) Plankton motility patterns and encounter rates. *Oecologia*, **148**, 538–546.

Koehl M.A.R., Jumars P.A., Karp-Boss L. (2003) Algal physics. In: Norton T.A. (Ed.), *Out of the Past*. British Phycological Association, Belfast: 115–130.

Kolmogorov A.N. (1941) Dissipation of energy in a locally isotropic turbulence. *Doklady Akademii Nauk SSSR*, **32**, 16–18.(English translation in Proceedings of the Royal Society of London A 434: 15-17, 1991)

Lamb H. (1932) *Hydrodynamics*. Cambridge University Press, Cambridge.

Latz M.I., Case J.F., Gran R.L. (1994) Excitation of bioluminescence by laminar fluid shear associated with simple Couette flow. *Limnology and Oceanography*, **39**, 1424–1439.

Lazier J.R.N., Mann K.H. (1989) Turbulence and diffusive layers around small organisms. *Deep-Sea Research*, **36**, 1721–1733.

Liao J.C., Beal D.N., Lauder G.V., Triantalyllou M.S. (2003) The Kármán gait: novel body kinematics of rainbow trout swimming in a vortex street. *Journal of Experimental Biology*, **206**, 1059–1073.

Lundgren T.S. (1982) Strained spiral vortex model for turbulent fine structure. *Physics of Fluids*, **25**, 2193–2203.

Marcos Stocker R. (2006) Microorganisms in vortices: a microfluidic setup. *Limnology and Oceanography: Methods*, **4**, 392–398.

Marcu B., Meiburg E., Newton P.K. (1995) Dynamics of heavy particles in a Burgers vortex. *Physics of Fluids*, **7**, 400–410.

Margalef R. (1978) Life-forms of phytoplankton as survival alternative in an unstable environment. *Oceanologica Acta*, **1**, 493–509.

Margalef R., Estrada M., Blasco D. (1979) Functional morphology of organisms involved in red tides, as adapted to decaying turbulence. In: Taylor D., Selinger H. (Eds), *Toxic Dinoflagellate Blooms*. Elsevier, New York: 89–94.

Monin A.S., Yaglom A.M. (1971) *Statistical Fluid Mechanics*, Vol. **1**, MIT Press, Cambridge, MA.

Munk W.H., Riley G.A. (1952) Absorption of nutrients by aquatic plants. *Journal of Marine Research*, **11**, 215–240.

Murray J.L.S., Jumars P.A. (2002) Clonal fitness of bacteria predicted by analog modeling. *BioScience*, **52**, 343–355.

Nowell A.R.M., Jumars P.A. (1987) Flumes: theoretical and experimental considerations for simulation of benthic environments. *Oceanography and Marine Biology, An Annual Review*, **25**, 91–112.

Pahlow M., Riebesell U., Wolf-Gladrow D.A. (1997) Impact of cell shape and chain formation on nutrient acquisition by marine diatoms. *Limnology and Oceanography*, **42**, 1660–1672.

Peskin C.S. (2002) The immersed boundary method. *Acta Numerica*, **11**, 479–517.

Peters F., Redondo J.M. (1997) Turbulence generation and measurement: application to studies on plankton. *Scientia Marina*, **61** (Suppl. 1), 205–228.

Petitjeans P. (2003) Stretching of a vortical structure: filaments of vorticity. *Europhysics News*, **34**, 20–23.

Pullin D.I., Saffman P.G. (1998) Vortex dynamics in turbulence. *Annual Review of Fluid Dynamics*, **30**, 31–51.

Ruiz J., Macías D., Peters F. (2004) Turbulence increases the average settling velocity of phytoplankton cells. *Proceedings of the National Academy of Sciences of the USA*, **101**, 17720–17724.

Saffman P.G. (1992) *Vortex Dynamics*. Cambridge University Press, Cambridge.

Sanford L.P. (1997) Turbulent mixing in experimental ecosystem studies. *Marine Ecology Progress Series*, **161**, 265–293.

Shimeta J., Jumars P.A., Lessard E.J. (1995) Influences of turbulence on suspension feeding by planktonic protozoa;

experiments in laminar shear fields. *Limnology and Oceanography*, **40**, 845–859.

Solari C.A., Ganguly S., Kessler J.O., Michod R.E., Goldstein R.E. (2006) Multicellularity and the functional interdependence of motility and molecular transport. *Proceedings of the National Academy of Sciences of the USA*, **103**, 1353–1358.

Squires K.D., Yamazaki H. (1995) Preferential concentration of marine particles in isotropic turbulence. *Deep-Sea Research*, **42**, 1989–2004.

Tallapragada P, Ross S.D. (2008) Particle segregation by Stokes number for small neutrally buoyant spheres in a fluid. arXiv:0801.3489v2 [nlin.CD] 12 Mar 2008.

Taylor G.I. (1921) Diffusion by continuous movements. *Proceedings of the London Mathematical Society*, **20**, 196–211.

Tennekes H., Lumley J.L. (1972) *A First Course in Turbulence*. MIT Press, Cambridge, MA.

Terray E.A., Donelan M.A., Agrawal Y.C., Drennan W.M., Kahma K.K., Williams A.J., Hwang P.A., Kitaigorodskii S.A. (1996) Estimates of kinetic energy dissipation under breaking waves. *Journal of Physical Oceanography*, **26**, 792–807.

Thomas W.H., Gibson C.H. (1990) Quantified small-scale turbulence inhibits a red tide dinoflagellate, *Gonyaulax polyedra* Stein. *Deep-Sea Research*, **37**, 1583–1593.

Thorpe S.A. (2007) *Introduction to Ocean Turbulence*. Cambridge University Press, Cambridge.

Tisalius P., Kuylenstierna B. (1996) Growth and decline of a diatom spring bloom [*sic,* punctuation missing] phytoplankton species composition, formation of marine snow and the role of heterotrophic dinoflagellates. *Journal of Plankton Research*, **181**, 133–155.

Tseng R.S., D'Asaro E. (2004) Measurements of turbulent vertical kinetic energy in the ocean mixed layer from Lagrangian floats. *Journal of Physical Oceanography*, **34**, 1984–1990.

Vaillancourt P.A., Yau M.K. (2000) Review of particle-turbulence interactions and consequences for cloud physics. *Bulletin of the American Meteorological Society*, **81**, 285–298.

Viitasalo M., Kiørboe T., Flinkman J., Pedersen L., Visser A. (1998) Predation vulnerability of planktonic copepods: consequences of predator foraging strategies and prey sensory abilities. *Marine Ecology Progress Series*, **175**, 129–142.

Visser A.W., MacKenzie B.R. (1998) Turbulence-induced contact rates of plankton: the question of scale. *Marine Ecology Progress Series*, **166**, 307–310.

Warnaars T.A., Hondzo M. (2006) Small-scale fluid motion mediates growth and nutrient uptake of *Selenastrum capricornutum*. *Freshwater Biology*, **51**, 999–1015.

Wu J.-Z., Ma H.-Y., Zhou M.-D. (2006) *Vorticity and Vortex Dynamics*. Springer, Berlin.

Yamazaki H. (1993) Lagrangian study of planktonic organisms: perspectives. *Bulletin of Marine Science*, **53**, 265–278.

Yokokawa M., Itakura K., Uno A., Ishihara T., Kaneda Y. (2002) *16.4-Tflops Direct Numerical Simulation of Turbulence by a Fourier Spectral Method on the Earth Simulator*. SC2002, Baltimore, MD.0-7695-1524-X/02